

# Spectroscopic Characterization and Imaging of Laser- and Unipolar Arc-induced Plasmas

Damien U.B. Aussems,<sup>1, a)</sup> Daisuke Nishijima,<sup>2</sup> Christian Brandt,<sup>2</sup> Russell P. Doerner,<sup>2</sup> and Niek J. Lopes Cardozo<sup>3</sup>

<sup>1)</sup>*FOM Institute DIFFER - Dutch Institute for Fundamental Energy Research, Nieuwegein, NL-3430 BE, the Netherlands*

<sup>2)</sup>*Center for Energy Research, University of California at San Diego, 9500 Gilman Drive, La Jolla, CA 92093-0417, USA*

<sup>3)</sup>*Science and Technology of Nuclear Fusion, Eindhoven University of Technology, Eindhoven, 5612 AZ, the Netherlands*

(Dated: 29 July 2014)

Tungsten plasmas induced by unipolar arcs were investigated using optical emission spectroscopy and imaging, and compared with laser-induced tungsten plasmas. The unipolar arcs were initiated in the linear-plasma simulator PISCES-A at UCSD under fusion relevant conditions. The electron temperature and density of the unipolar arc plasmas were in the range 0.5–0.7 eV and  $0.7\text{--}2.0 \times 10^{20} \text{ m}^{-3}$ , respectively, and increased with increasing negative bias voltage, but did not correlate with the surface temperature. In comparison, the electron temperature and density of the laser-induced plasmas were in the range 0.6–1.4 eV and  $7 \times 10^{19}\text{--}1 \times 10^{22} \text{ m}^{-3}$ , respectively.

## I. INTRODUCTION

Tungsten will be used as fusion wall material in the high heat flux region (e.g. the divertor) of ITER, because of its high melting point (3695 K), high thermal conductivity ( $173 \text{ W m}^{-1} \text{ K}^{-1}$ ), and high sputtering threshold (216 eV for D-impact). Recent experiments show that ‘fuzz’ - nano-scale structures (porosity  $\sim 90\%$ ) - is formed on the tungsten surfaces when it is exposed to helium plasmas and even occur when the incident ion energy is less than the threshold energy for physical sputtering<sup>1</sup>.

An equilibrium model for fuzz growth and erosion indicates that fuzz can grow in tokamaks<sup>2</sup>. In fact, the growth of fuzz has recently been observed in the divertor of the Alcator C-Mod tokamak<sup>3</sup>. Recent studies have shown that transient heat loads on the divertor such as ELMs might trigger unipolar arcing, and that fuzz significantly increases its ignition<sup>4</sup>.

The existence of the unipolar arc has been confirmed phenomenologically by erosion craters found in numerous fusion devices: JT-60U, LHD<sup>5</sup>, DIII-D<sup>6</sup>, and ASDEX Upgrade<sup>7,8</sup>. Moreover, since the arcing may take place in fusion experiments, special model experiments have been conducted for a systematic study in which arcing is initiated by plasmas generated by a high-frequency discharge<sup>9,10</sup>, a plasma gun<sup>11,12</sup>, and a laser beam<sup>13,4,14</sup>.

What is missing is an investigation into the properties of (unipolar) arc-induced plasma, which requires proper diagnostics. This research uses the transient heat load of a laser-pulse to trigger unipolar arcing on fuzzy tungsten and has the aim to spectroscopically characterize the arc-induced plasma. Since in our research the laser pulse is essential for the ignition of arcing, this research

also includes an analysis of laser-induced plasma and a comparison between the two types of plasma.

Spectroscopical characterization of plasmas induced by laser irradiation on a surface has been performed previously (mostly to analyze the surface composition) and is also referred to as laser-induced breakdown spectroscopy or LIBS (Refs. 15,16 discuss LIBS on tungsten surfaces). The approach adopted in this research is to use optical emission spectroscopy not only for laser-induced plasma, but for arc-induced plasma as well.

In this work, the intensities of the atomic emission lines are measured, and the Boltzmann and Saha-Boltzmann relations are used for the evaluation of the electron temperature and density<sup>17</sup>. This theory is further explained in Sec. II. The optical emission spectroscopy setup is devised and used to investigate laser-induced tungsten plasma, which results are discussed in Sec. III. These experiments also function as benchmark for the spectroscopy system. Next, the setup is moved to the linear divertor plasma simulator PISCES-A to analyze arc-induced tungsten plasma. These results are discussed in Sec. IV. In the end, the laser- and arc- induced plasma experiments are compared and conclusions are drawn in Sec. V.

## II. THEORY

During the expansion phase of laser-induced and unipolar arc plasmas, volume recombination occurs. This is identified by typical spectral emission: continuum emission due to free-bound transitions (radiative recombination) and line emission from highly excited levels (three-body recombination). Both processes are often classified as electron-ion recombination (EIR).

The line emission represents the number of recombination processes and hence the population density of spe-

---

<sup>a)</sup>Electronic mail: [d.aussems@diffier.nl](mailto:d.aussems@diffier.nl)

cific states. These population densities can be used to estimate the excitation temperature  $T$  of the plasma by the Boltzmann relation<sup>18</sup>

$$\frac{n_n}{n_m} = \frac{g_n}{g_m} \exp\left(-\frac{E_n - E_m}{kT}\right), \quad (1)$$

where  $n_n$ ,  $n_m$ ,  $g_n$ ,  $g_m$ ,  $E_n$  and  $E_m$  are the population densities, the statistical weights and the energies of the atomic states  $n$  and  $m$ ,  $k$  is the Boltzmann constant.

The relation is only valid for the population of atoms under partial local thermodynamic equilibrium (PLTE), or equivalently, the population of atoms with excited levels<sup>18</sup>

$$n > n_{cr} = \left[ \frac{10}{2\sqrt{\pi}} \frac{z^7}{n_e} \frac{\alpha^3}{a_0} \right]^{2/17} \left( \frac{kT}{z^2 E_H} \right)^{1/17}, \quad (2)$$

in which  $z$  is the effective nuclear charge ( $z = 1$  for neutral atoms),  $\alpha$  is the fine structure constant ( $\alpha = 1/137$ ),  $a_0$  the Bohr radius ( $a_0 = 5.3 \times 10^{-11}$  m) and  $E_H$  the ionization energy of hydrogen atom ( $E_H = 13.6$  eV). Under PLTE, the excitation temperature can be assumed equal to the electron temperature  $T_e$ . For our typical plasma ( $n_e = 10^{20}$  m<sup>-3</sup>,  $T_e = 1$  eV), equation (2) gives  $n_{cr} = 4$ .

An example of a typical intensity spectrum of a tungsten plasma (in this case of a unipolar arc) is shown in Fig. 1, in which the red lines are the used transition lines. The wavelength, upper and lower energy, Einstein coefficient, and statistical weight per transition line can be found in the NIST database<sup>19</sup> and are summarized in Tab. I. As can be seen, the quantum number of the excited states from the list of transition lines are well above  $n_{cr}$  (the ground states are already  $n > 5$ ).

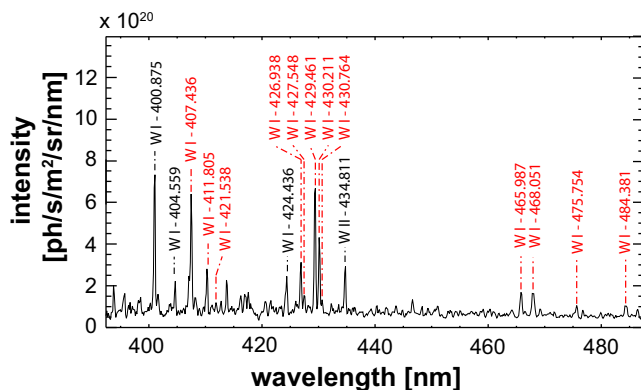


FIG. 1. Typical electron-ion recombination (EIR) intensity spectrum (5 ms exposure time, 100  $\mu$ s delay time) of tungsten plasma induced by an unipolar arc ( $n_e = 2 \times 10^{20}$  m<sup>-3</sup>,  $T_e = 0.7$  eV). The red lines indicate the used transition lines, and the other lines are either other EIR transition lines (black) or impurities (H, O, La, B, or C). Not all transition lines are used, because some did not consistently appear for each shot.

The population density of the upper transition levels  $n_n$  in Equation (1) is calculated from the measured intensities of the transitions<sup>18</sup>

$$n_n = \frac{4\pi}{A_{nm}L} I_{nm}, \quad (3)$$

with  $A_{nm}$  the Einstein coefficient for spontaneous emission,  $L$  the plasma depth, and  $I_{nm}$  the emission intensity in [phs<sup>-1</sup>m<sup>-2</sup>sr<sup>-1</sup>]. Figure 2 shows a typical population distribution as a function of the upper state energy  $E_n$ . The slope of the linear fit provides the electron temperature.

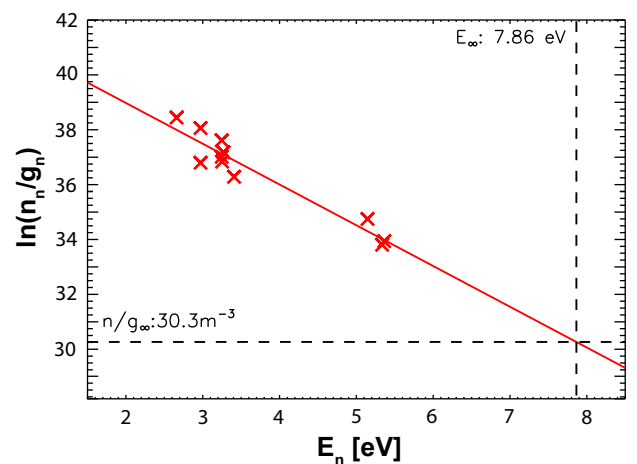


FIG. 2. Typical Boltzmann plot of tungsten emission in which the population density of the upper transition levels  $n_n$  divided by the degeneracy  $g_n$  of the upper state are plotted as function of the upper energy level  $E_n$ . The data is fitted with a linear regression method, and from this data the electron temperature and density are determined. The slope provides information of the electron temperature ( $T_e = -1/\text{slope}$ ), and the electron density can be determined from the intersect with the ionization limit  $E_\infty$  (horizontal dashed line). The scattering in the data provides the uncertainty of the measurement, which is less than 10 % in this case.

Next, we can calculate the electron density by using the Saha-Boltzmann equation, and assuming that  $W^+$  is dominant and thus that  $n_e$  equals  $n_i$ <sup>18</sup>:

$$\frac{n_e n_i}{n_n} = \frac{2g_i}{g_n a_0^3} \left( \frac{kT_e}{4\pi E_H} \right)^{3/2} \exp\left(-\frac{E_{ni}}{kT_e}\right), \quad (4)$$

in which  $E_{ni} = E_\infty - E_n$  is the ionization energy of the particle state  $n$ . The statistical weight  $g_i$  for the ion is 2 for the ground state of  $W^+$ . The ratio  $n_n/g_n$  for  $E_{ni} = 0$  eV can be determined by extrapolating to the ionization limit  $E_\infty = 7.86$  eV for W.

It is possible that  $W^{2+}$  could be dominant. In that case the electron density would be a factor  $\sqrt{2}$  higher than assumed, and the density criteria Eq. 2, would be more easily met.

TABLE I. This electron-ion recombination transition lines are used to measure the electron temperature and density of laser-induced and arc plasmas. The table includes the transition wavelength  $\lambda$ , lower and the upper energy state, the degeneracy  $g_n$  of the upper state, and the Einstein coefficient  $A_{nm}$  for each line.

$\lambda$ [nm]	Transition		Energy [eV]		$g_n$	$A_{nm}$ [ $s^{-1}$ ]
	Lower	Upper	Lower [eV]	Upper [eV]		
407.436	5d <sup>5</sup> (6S)6s	5d <sup>5</sup> (6S)6p	0.36591	3.40809	7	1.0 · 10 <sup>7</sup>
411.805	5d <sup>5</sup> (4G)6s	-	2.35254	5.36244	9	9.3 · 10 <sup>6</sup>
421.538	5d <sup>5</sup> (4G)6s	-	2.42203	5.36244	9	3.7 · 10 <sup>6</sup>
426.938	5d <sup>5</sup> (6S)6s	-	0.36591	3.26913	5	3.0 · 10 <sup>6</sup>
427.548	5d <sup>5</sup> (4G)6s	-	2.24620	5.14527	7	9.3 · 10 <sup>6</sup>
429.461	5d <sup>5</sup> (6S)6s	5d <sup>5</sup> (6S)6p	0.36591	3.25208	5	1.2 · 10 <sup>7</sup>
430.211	5d <sup>5</sup> (6S)6s	5d <sup>4</sup> 6s(6D)6p	0.36591	3.24705	7	3.6 · 10 <sup>6</sup>
430.764	5d <sup>4</sup> 6s <sup>2</sup>	-	2.45812	5.33555	11	5.4 · 10 <sup>6</sup>
465.987	5d <sup>4</sup> 6s <sup>2</sup>	5d <sup>4</sup> 6s(6D)6p	0.00000	2.65994	3	1.0 · 10 <sup>6</sup>
468.051	5d <sup>4</sup> 6s <sup>2</sup>	5d <sup>4</sup> 6s(6D)6p	0.59884	3.24705	7	1.4 · 10 <sup>6</sup>
475.754	5d <sup>5</sup> (6S)6s	5d <sup>4</sup> 6s(6D)6p	0.36591	2.97124	5	2.7 · 10 <sup>5</sup>
484.381	5d <sup>4</sup> 6s <sup>2</sup>	5d <sup>4</sup> 6s(6D)6p	0.41231	2.97124	5	1.9 · 10 <sup>6</sup>

In order to determine whether  $T_e$  and  $T_i$  are equal, we have to investigate if the local thermodynamic equilibrium (LTE) is satisfied. This equilibrium requires that the atomic and ionic states are populated and depopulated predominantly by electron collisions rather than by radiation. It also requires an electron density sufficient to endure a high collision rate. The electron density to achieve LTE in a plasma is given by the McWhirter criterion<sup>20</sup>

$$n_e > 1.6 \times 10^{18} \times T_e[\text{K}]^{1/2} E[\text{eV}]^3, \quad (5)$$

where  $E$  is the difference in energy between upper and lower level transitions and  $T_e$  is the plasma temperature. If  $E$  approaches 5 eV, and  $T_e = 2$  eV (maximum measured temperature), the electron density needed to satisfy LTE is  $2.8 \times 10^{20} \text{ m}^{-3}$ . Our measured  $n_e$  is above this number for most of the data points. In the case when the LTE approximation is not valid,  $T_e$  and  $T_i$  might disperse. If we consider that the electrons are the mobile charges which transfer the energy to the heavy ions, we can say that in those case  $T_e \gg T_i$ .

### III. LASER-INDUCED PLASMA

The interaction of laser irradiation with a metal surface can lead to the removal of material from the surface, so-called laser ablation. For sufficiently high laser power, the material undergoes an explosive phase transition from solid into plasma by underlying processes such as sublimation, evaporization and ionization<sup>21</sup>. During the laser pulse continuum and ion emission appears and lasts for several hundred nanoseconds, while atomic line emission appears during the plasma expansion phase ( $> 1 \mu\text{s}$ ). From the latter the electron temperature and density of the laser-induced tungsten plasma can be determined.

## A. Experimental Setup

### 1. Setup and Diagnostics

To investigate the electron temperature and density of laser-induced plasma a gas chamber is used in which the pressure can be varied. The chamber is pumped by a rotary vane pump [Edwards, Model RV12], and a minimum base pressure of  $3 \times 10^{-3}$  mbar is achieved. The pressure can be varied from this base pressure up to atmospheric pressure. The sample is installed in the chamber, and hit by a 1064 nm Nd-YAG laser with power density of  $7.4 \times 10^{13} \text{ Wm}^{-2}$  (6 ns pulse width) to initiate a plasma. The beam is focused on the target at normal incidence using an antireflection-coated plano-convex lens, reaching a spot size of 1 mm.

Figure 3 illustrates the experimental setup. The emission of the plasma plume is collected by a lens and fiber optical system into a spectrograph [Spectra-Pro 2300i] with a 600 grooves/mm grating. The exit port of the spectrograph is coupled to an intensified charged coupled device [(ICCD) PI MAX, Model EEV]. The dispersion at the wavelength range used is 0.1334 nm/px. Another ICCD camera [PI MAX, Model THM,  $512 \times 512$  px] is used to capture a two-dimensional image of the plume emission in order to estimate the emission area, and the plasma depth.

### 2. Absolute Intensity Calibration

In order to measure the absolute emission spectrum, the spectrometer is calibrated with an integrating sphere calibration standard (Optronic Laboratories, Model OL-455-12-1), which consists of a source module containing a 150 W tungsten-halogen reflectorized lamp with a known spectrum. The spectrum correction factor is defined as  $K_{int}(\lambda) = I_{int}(\lambda)/I_{m,int}(\lambda)$ , in which  $I_{int}(\lambda)$  and  $I_{m,int}(\lambda)$  are the manufacturer and measured spectrum

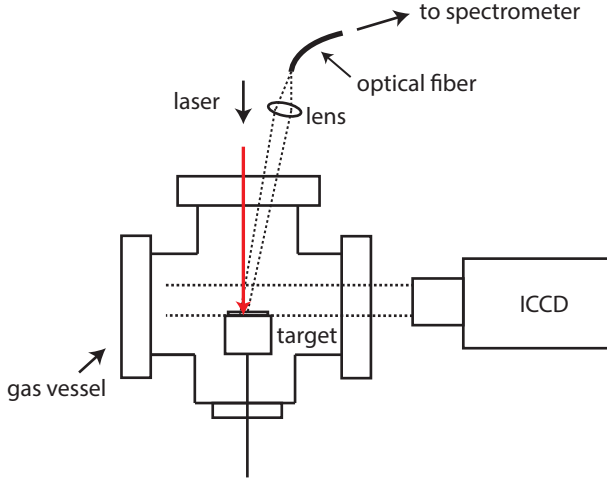


FIG. 3. The experimental setup: a laser hits a tungsten target in a vacuum chamber. An optical lens and fibre system is used to collect the emission from the laser shot into a spectrometer. An ICCD camera is used to determine the emission area, and the plasma depth.

of the integrating sphere, respectively. Moreover, an area correction factor  $K_A = A_{lens}/A_{emis}$  is introduced since the emission area from the plasma  $A_{emis}$  is likely to disperse from the area collected by the lens column  $A_{lens}$ . The total calibration function is given by:

$$I_a(\lambda)[\text{ph s}^{-1}\text{m}^{-2}\text{sr}^{-1}\text{nm}^{-1}] = K_{\text{int}}(\lambda)K_A I_m(\lambda) \quad (6)$$

where  $I_m(\lambda)$  is the measured intensity of a plasma calculated by  $I_m(\lambda) = n_{ph}/t_p$ , in which  $n_{ph}$  is the number of counted photons and  $t_p$  is the duration of the plasma.

### 3. Plume Observation

The laser-induced ablation plumes are visualized by ICCD images as function of the delay time to gain a better understanding of the expansion dynamics. This is depicted in Fig. 4. A tungsten plasma is initiated and expands as function of time. The plume is characterized by turbulent structures, and after a few microseconds the expanding plume has considerably decelerated and starts diffusing in the background gas. For helium the expansion appears to be faster and the diffusion to be larger compared to argon and air. Eventually the plume will come to rest due to collisions with the background gas.

The expansion can be understood in the theoretical framework of an expansion and drag model, discussed in Ref. 22. The faster plume expansion in helium than in argon and air, can be explained by the larger collisional cross section of argon and air compared to helium.

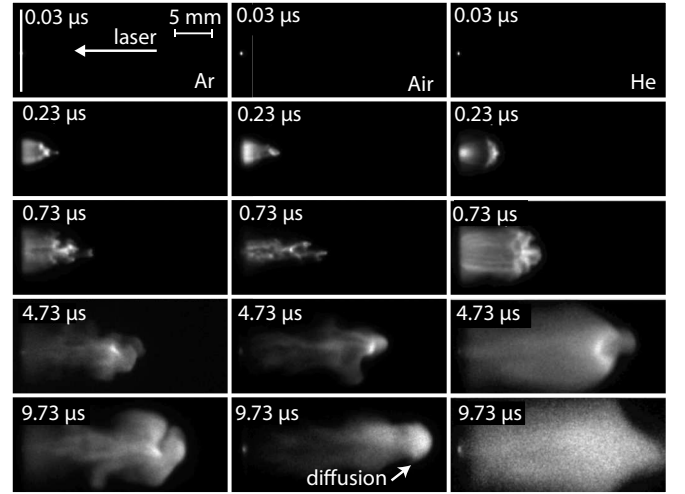


FIG. 4. Time evolution of visible light emission from a tungsten plume with Ar, Air, and He background recorded using an ICCD camera. Each image is taken from a single laser shot and reproducible. The exposure time used was 1 ns. The laser power density was  $7.4 \times 10^{13} \text{ Wm}^{-2}$  (6 ns pulse width), and the background pressure was 13 mbar. The timings in the images represent the time after the onset of plasma formation. All images are normalized to their maximum intensity. In general the plasma expands, and a plume is formed.

### 4. Determination of Emission Area and Plasma Depth

Essential for the measurement of the electron density and temperature are the emission area and plasma depth, which are determined using the ICCD camera. Figure 5 shows an example of an ICCD image of a tungsten plume. The side-view plasma emission area  $A_{plasma}$  is defined as the area with an intensity exceeding  $1/e \times I_{max}$ . From  $A_{plasma}$  the emission area radius  $r_{emis}$  is calculated by a Gaussian fit of the z-integrated intensity and subsequently the emission area  $A_{emis} = \pi r_{emis}^2$ . The plasma depth (z-length) is determined by  $L = A_{plasma}/(2 \times r_{emis})$ .

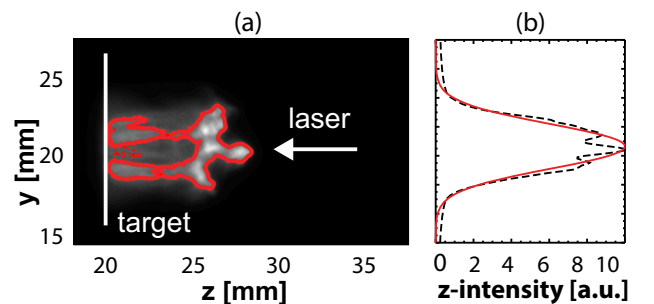


FIG. 5. a) ICCD emission image of tungsten plume. The red line covers the area  $A_{emis}$ . b) z-integrated emission profile (black dashed line). From the FWHM of the Gaussian fit (red line) the emission area radius is calculated, and subsequently the plasma depth.

## B. Results

In order to test the diagnostic the electron temperature and density were determined as function of the pressure. Since the emission of the plasma also depends on the nature of the background gas<sup>23</sup>, three different background gases were used.

The results of the electron temperature and density measurements of laser-induced tungsten plasma as function of the pressure is presented in Fig. 6. The delay time is  $0.73\mu\text{s}$  and the exposure time is  $100\mu\text{s}$ . The laser power density was  $7.4 \times 10^{13} \text{ Wm}^{-2}$  (6 ns pulse width). Each data point represents the average of three measurements (uncertainty is calculated from the uncertainty from the single data points). In general, the electron density and temperature show an increase with an increasing pressure above 0.2 mbar.

Figure 7 shows that at pressures below 0.2 mbar plasma diffuses from the target into the gas. In the pressure range ( $0.2 \text{ mbar} < p < 4 \text{ mbar}$ ) several interesting phenomena are observed. First of all shock waves formations can be observed. At pressure around  $\sim 0.3 \text{ mbar}$ , the faster moving component of the expanding plume front splits into two clouds, which is referred to as plume splitting<sup>22</sup>. At slightly higher pressures ( $\sim 0.4 \text{ mbar}$ ), the plume front is spherical in nature at first, but as time evolves the plume front sharpens. Plume sharpening behavior suggests that higher kinetic energy particles are emitted closer to the target surface normal<sup>22</sup>. At pressures above 0.4 mbar, the contact boundary of the shockwave starts to show instabilities<sup>24</sup>. At relatively high pressures ( $> 4 \text{ mbar}$ ), the plasma shows a high confinement and plume ejection is observed. Moreover, the plume appears to be ejected in a direction perpendicular to the surface.

## C. Discussion

The electron temperature and density of laser-induced plasmas are found to be in the range of  $0.6\text{--}1.4 \text{ eV}$ , and  $7 \times 10^{19} - 1 \times 10^{22} \text{ m}^{-3}$ , respectively (same range as Ref. 16). The spectrometry setup was proved reasonably accurate in measuring electron temperature (20 % relative error) but rather rough in measuring the electron density (factor 2).

It has to be noted that these quantities were measured using an exposure time ( $\Delta t$ ) of the ICCD camera of  $100\mu\text{s}$ , which is relatively long compared to the (fixed) delay time of  $0.73\mu\text{s}$ . This means that the actual values of  $T_e$  and  $n_e$  at precisely the delay time are different from our measured, time-averaged values. The effect of this on  $T_e$  is only marginal, however. This is because the relative proportion between the intensities from the emission lines depends on the total collected light ( $I_{tot}$ ), which

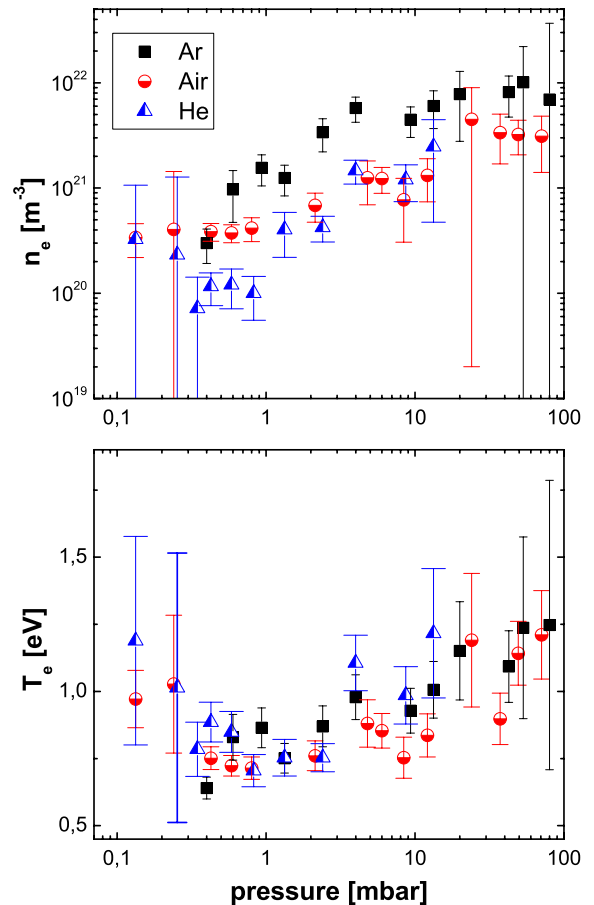


FIG. 6. Electron density and temperature of a tungsten plasma with Ar, Air, and He background as function of the pressure. The exposure time is  $100\mu\text{s}$ , and the delay time was  $0.73\mu\text{s}$ . The laser power density was  $7.4 \times 10^{13} \text{ Wm}^{-2}$  (6 ns pulse width). The results show that electron temperature and density increase with increasing pressure. At pressures below 0.3 mbar the uncertainty in the measurement is high.

predominantly ( $> 60\%$ ) originates within the first few microseconds after the start of the measurement due to the exponential decay. On the other hand,  $n_e$  is affected by  $n_e \sim \sqrt{I}$ . Because the majority of the light is emitted within the first few microseconds - around 50 times shorter than the integration time - the measured intensity ( $I_{tot}/\Delta t$ ) is underestimated compared to the actual intensity by  $\sim 50$  times. This means that the actual  $n_e$  is expected to be around 7 times higher than measured.

The data shows that a pressure increase leads to a rise in the electron temperature and density. In our pressure range ( $> 0.4 \text{ mbar}$ ) this can be explained by the higher confinement of the plasma for higher pressures (similar results as Ref. 15). A higher confinement can also be observed in the ICCD images of Fig. 7. At pressures below 0.3 mbar, both the electron temperature and density show a large uncertainty. This might be related to the transition of the plasma - background gas interaction from collisional to collisionless, so the plasma

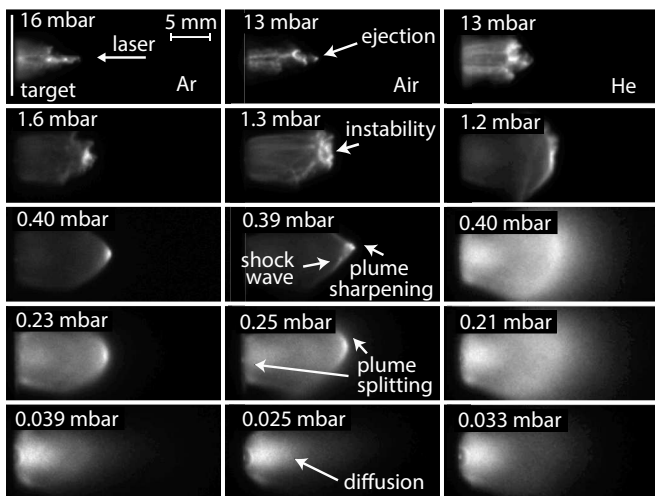


FIG. 7. Pressure scan of visible light emission from a tungsten plume with Ar, Air, and He background recorded using an ICCD camera (images are reproducible). The exposure time used was 1 ns, and delay time 0.73 $\mu$ s. The laser power density was  $7.4 \times 10^{13} \text{ Wm}^{-2}$  (6 ns pulse width). All images are normalized to their maximum intensity. Depending on the pressure plume sharpening, splitting, ejection and diffusion, and shockwave formations can be observed.

is insufficiently confined for spectroscopy.

In general, the data suggests that tungsten plasmas generated in the He ambient are slightly hotter than for the Ar ambient. This is in contrast to previous reports on laser ablation on Fe, which shows that He acts as an effective coolant in comparison to Ar or Air<sup>25</sup>. While the material and pressure range from this work is different, it is still expected that this would be the case in our experiment as well. The plasma measurement for He is possibly affected by our measurement method. In the case of He, the peaks of the transition lines with high transition energies ( $\sim 5$  eV) are relatively low. These peaks are thus easily affected by noise. When the noise is relatively high, the intensity of the high energy transition lines is enhanced, which 'tilts' the Boltzman fit towards a higher measured electron temperature and density.

#### IV. ARC-INDUCED PLASMA

Unipolar arcing is a discharge between the plasma and the wall and may occur in plasma devices, e.g. tokamaks. This phenomenon features localized, bright, tiny ( $\sim 1 \mu\text{m}$ ) spots on the wall surface. The process is ignited by a dense primary erosion plasma due to an external action (e.g. a laser pulse or ELM-plasma) onto the target. The dense plasma in combination with the nano-protrusions of the tungsten fuzz can locally amplify the electron emission and thus input energy (the start of an emission spot). At these spots the wall material makes an explosive transition into dense plasma, which then ex-

pands rapidly into the vacuum. This dense plasma is a key factor in unipolar arcing, as it provides the conditions for new and hence repetitive ignition of micro-explosions, while on the other hand 'choking' the already operating emission center by its limited conductivity. Similarly as with laser-induced plasmas, line radiation is emitted during the expansion phase of the micro-explosion<sup>26</sup>, which enables us to measure the electron density and temperature of the unipolar arc plasmas.

#### A. Experimental Setup

##### 1. Linear divertor plasma simulator PISCES-A

In order to study arcing in fusion relevant conditions we use the PISCES-A experiment. The device consists of a 2.5 m long, 20 cm diameter stainless steel cylindrical vacuum chamber that is pumped by two turbo molecular pumps to control the gas pressure. A typical base pressure of  $9 \times 10^{-7}$  mbar can be reached. Large viewing ports provide access for diagnostics.

The plasma is produced by a reflex arc discharge from a large (diameter = 7.6 cm) heated lanthanum hexaboride (LaB<sub>6</sub>) disc cathode to a cooled cylindrical anode<sup>27</sup>. The continuously operating plasma source is about 50 cm long, and produces a 7.5 cm diameter plasma which is confined by a 0.094 T solenoidal magnetic field. The plasma density and electron temperature are measured by a Langmuir probe, which is inserted into the plasma by a pneumatic plunging system<sup>28</sup> that scans the radial plasma profile. The values for  $n_e$  and  $T_e$  are typically  $> 10^{18} \text{ m}^{-3}$  and 5–7 eV, respectively. The plasma flows along the magnetic field to the target where the ions are accelerated by a sheath potential on an electrically biased target, producing an ion flux on the order of a few  $10^{22} \text{ m}^{-2}\text{s}^{-1}$  with an energy that can be controlled between 50–250 eV. The ion-energy distribution function at the surface is non-thermal, with an energy width ( $\sim 1$  eV) that is small compared with the mean ion energy. The ions have normal incidence with respect to the surface.

The target is installed on an Inconel sample manipulator which can be moved in axial direction. The target is cooled by pressurized air, which flow can be varied. A sample temperature of 1020–1270 K was achieved in this experiment.

##### 2. Arc ignition

Figure 8 illustrates the experimental setup. First, a fuzz layer ( $\sim 1 \mu\text{m}$ ) was created by exposing the target to a He-plasma for 1 hr, while its surface temperature was controlled by air cooling and target biasing. The ion flux was  $2\text{--}5 \times 10^{22} \text{ m}^{-2}\text{s}^{-1}$ , and the surface temperature was  $\sim 1200$  K. The bias voltage was  $-100$  V in campaign 1, and  $-60$  V in campaign 2.

Immediately before arc initiation (He plasma is present), the sample temperature and bias voltage are varied. A 1064 nm Nd-YAG laser with a power density of  $7.4 \times 10^{13} \text{ Wm}^{-2}$  (6 ns pulse width) is used to initiate arcing (see introduction Sec. IV). The laser beam is focused on to the sample with a lens and directed with an angle of  $\sim 15^\circ$  from the surface normal using a mirror inside the vessel, reaching a spot size of 1 mm.

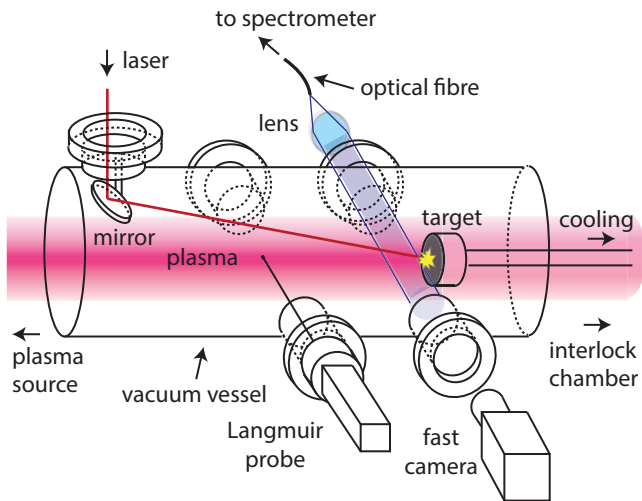


FIG. 8. Illustration of the arcing experiment. A tungsten target is exposed to helium plasma and a fuzz layer is grown. The laser hits the fuzzy tungsten target and arcing is initiated if the conditions are within the parameter space for arcing.

### 3. Arc Diagnostics

The emission of the arcing plasma is collected by a lens and fibre optical system into the same spectrograph used in the laser-induced plasma experiment (see Sec. III A 1). A fast camera (Phantom I,  $8.2 \mu\text{s}$  repetition rate,  $7.9 \mu\text{s}$  exposure time,  $256 \times 160$  px) is used to determine the emission area and plasma depth. The spectrometer system and fast camera are triggered by the output 'sync' signal of the Nd-YAG laser. The transient current during arcing is measured by a Pearson current monitor (Model 3972), which is installed between the target and the ground.

### 4. Arc Observation

The ignition and propagation of a typical arc is visualized by fast camera images (exposure time is  $7.8 \mu\text{s}$ ). For delay times above  $\sim 50 \mu\text{s}$  the laser-induced plasma has been expanded/diminished and the unipolar arc plasma becomes dominant. After ignition, the arc spot starts to randomly move around the surface, splits into two emission sites at  $\sim 300 \mu\text{s}$  and extinguishes at 2.9 ms. The arc terminates either because the fuzz is already damaged

by previous emission sites or the expanded plasma has choked the ignition of new sites. In general, the arcs have an duration of 2–6 ms and sustain a current of 20–70 A.

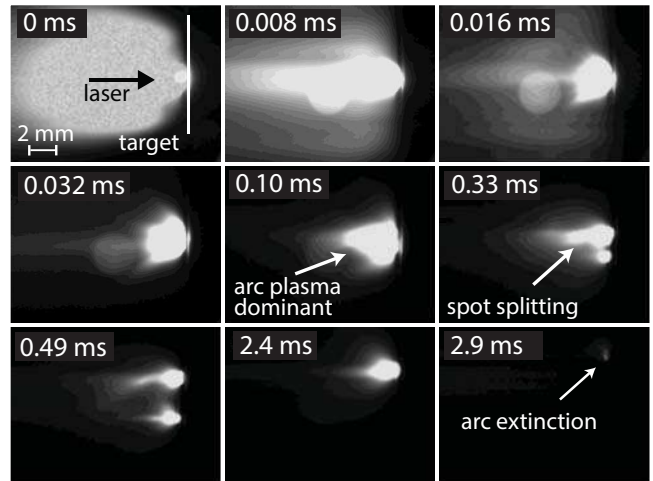


FIG. 9. Time lapse images of arcing measured by a fast camera. The arc is initiated by a laser pulse on a tungsten target with a fuzzy tungsten top-layer.

### 5. Determination of Emission Area and Plasma Depth

Similar to the laser-induced plasma experiments, the emission intensity was corrected using Eq. 6. A typical image of an unipolar arc is depicted in Fig. 10 ( $t_{\text{delay}} = 410 \mu\text{s}$ ,  $t_{\text{exposure}} = 7.9 \mu\text{s}$ ). In this case there are at least two emission sites. This number of parallel-operating emission sites can be related to the arc current<sup>26</sup>.

The effective emission area  $A_{\text{emis}}$  is approximated as the area in which the intensity exceeds  $1/e \times I_m$ , where  $I_m$  is the maximum intensity (on average measured value is  $50 \pm 30 \text{ mm}^2$ ). The total integrated intensity was divided by the arc duration. By considering axial symmetry and assuming a spherical plasma shape, the plasma depth  $L$  (x-length) can be first-order estimated as  $\sqrt{A_{\text{emis}}/\pi}$ .

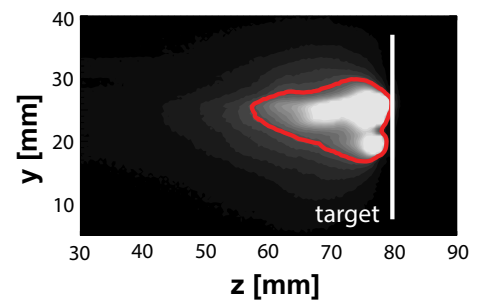


FIG. 10. Fast-camera image of arc emission spot at  $t = 410 \mu\text{s}$ , and the exposure time is  $7.9 \mu\text{s}$ . The red line shows the effective emission area  $A_p$  in which the emission exceeds  $1/e \times I_m$ .

## B. Results

The bias voltage dependence of the electron temperature and density is depicted in Fig.11. The exposure time was 5 ms and the delay time 500  $\mu$ s. The data was gathered in two campaigns. The data of both campaigns suggests that the electron temperature and density increase with increasing negative bias voltage,  $V_b$ .

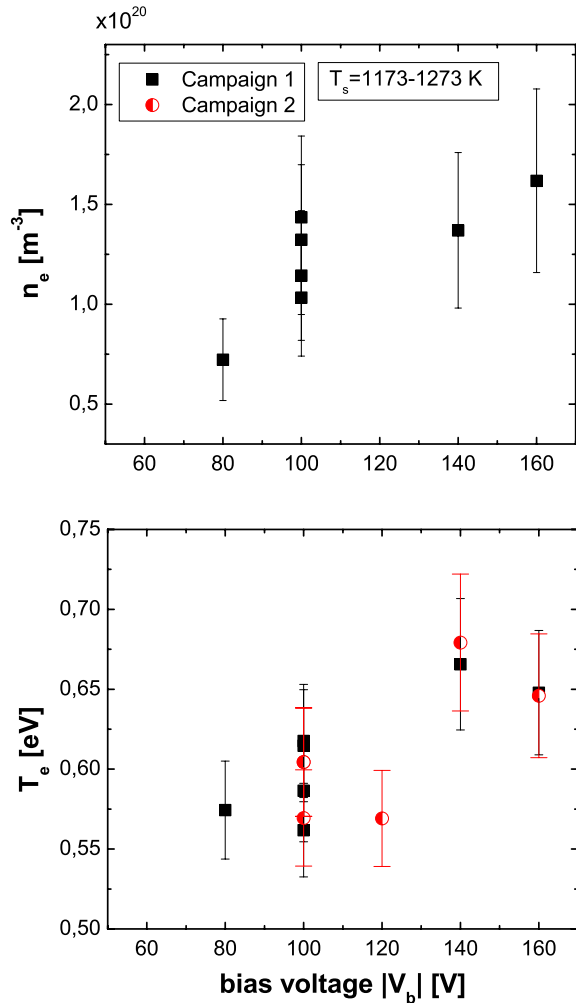


FIG. 11. Electron density and temperature as function of the bias voltage  $V_b$  (absolute value). The electron density and temperature of the arc plasma appear to increase with increasing negative bias voltage.

The sample temperature dependence of the electron temperature and density is shown in Fig. 12. The exposure time was 5 ms, and the delay time 500  $\mu$ s. For sample temperature  $> 970$  K, the graph shows that the electron temperature is not correlated with the sample temperature. The data point at 870 K and 970 K are questionable, since we could not reach the low sample temperature by cooling, and had to switch off the plasma, and turn it back on again. When we turned on the plasma, the temperature was slowly increasing, and we shot the laser when the temperature was within the set-

ting for that specific experiment. Since the temperature increased sufficiently slowly, we assumed that the plasma was in quasi steady-state.

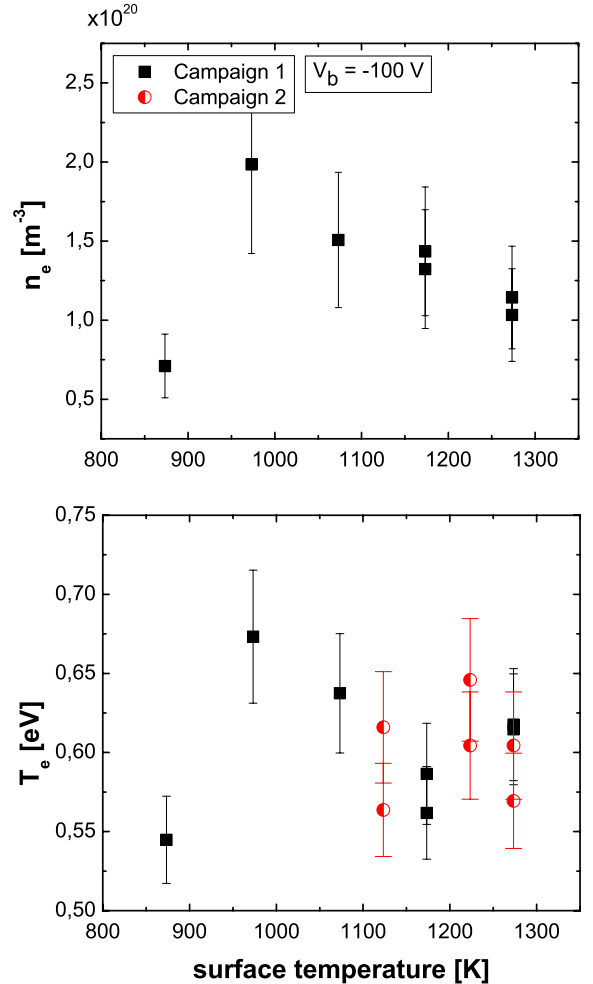


FIG. 12. Electron density and temperature as function of the sample temperature. The electron density and temperature appear to be effected for lower sample temperatures.

## C. Discussion

The electron temperature and density of arc plasmas were measured as function of the bias voltage and sample temperature using spectroscopy in combination with (fast camera) emission images. The values of the electron temperature and density were in the range 0.5 – 0.7 eV, and  $0.7 - 2.0 \times 10^{20} \text{ m}^{-3}$ , respectively. The relative uncertainty was on average 10% and 34%, respectively. Although arcing is a random process, the spectroscopic data fits in between the error bars, indicating consistency.

In the case of the arc and laser-induced plasma, the measured electron density and temperature of the plasma are spatially and temporally averaged. It is interesting to note that the uncertainty in these plasma param-

ters is significantly higher in comparison with the laser-induced plasma experiments. A possible explanation is that the arcs are characterized by plasma formation due to multiple micro-explosions hence ‘samples’, in comparison to the single explosion thus sample of the laser-induced plasma (the uncertainty of the measurement is proportional to  $1/\sqrt{N}$ , in which  $N$  is the number of samples).

The electron temperature of the arc plasma is one order of magnitude lower than the temperature of the surrounding helium plasma supplied by the discharge power supply (5–7 eV), while the electron density of the arc plasma is two order of magnitude higher. It has to be noted that the electron temperature and density may be significantly higher at a local spot right after an explosion, compared to the measured temporal and spatially averaged value.

The data suggests that the electron temperature and density increase with increasing negative bias voltage. The increase can be related to the energy dissipation during arcing, which increases with a higher bias voltage and can be expressed as<sup>26</sup>:  $E_{arc} = I_{arc}V_{arc}\tau$ , in which  $I_{arc}$  is the arc current,  $V_{arc}$  the arc voltage (proportional to the bias voltage), and  $\tau$  the time interval over which averaged. This energy is mostly transferred to heat the cathode, to emit and heat electrons and to produce and accelerate ions, which leads to a higher electron temperature and density.

Concerning the sample temperature dependence, for sample temperatures above 970 K, there is no clear trend as function of the sample temperature. This is also expected for the following reason: when a micro explosion occurs, the local density increases, which significantly enhances the local electric field and hence ion bombardment of that spot and the nearby emission spots. This leads to enhanced electron emission and heating at the nearby emission spots. The temperature of these spots is significantly higher than the sample temperature away from this local spot.

## V. SUMMARY AND CONCLUSIONS

Tungsten arc-plasma was investigated using optical emission spectroscopy and imaging in the linear divertor-plasma simulator PISCES-A at UCSD. As a comparison and benchmark of the spectroscopic system, laser-induced tungsten plasmas were also investigated.

The electron temperature and density of the unipolar arc plasma were in the range 0.5–0.7 eV and  $0.7\text{--}2.0 \times 10^{20} \text{ m}^{-3}$ , respectively. The electron temperature and density of the arc-induced plasma appear to increase with increasing negative bias voltage, which can be explained by the increase of the energy dissipation during the arc for higher bias voltages. The surface temperature was not found to influence the arc-induced plasma. A possible explanation is that when the arc is burning, the temperature of the emission site is significantly higher

than the temperature of the surrounding surface.

The electron temperature and density of the laser-induced plasmas were found to be in the range of 0.6–1.4 eV, and  $7 \times 10^{19} - 1 \times 10^{22} \text{ m}^{-3}$ , respectively.

Unipolar arc and laser-induced tungsten plasmas are initiated by explosive sublimation and/or evaporation, and ionization of the tungsten surface material. The underlying mechanisms that lead to these processes are different for both types of plasma. Nevertheless, the electron temperature and density of the unipolar arc plasmas overlap the lower limit of those of laser-induced plasmas.

If unipolar arcs occur in fusion reactors, optical emission spectroscopy can be a useful diagnostic to characterize the unipolar arc plasma.

## ACKNOWLEDGMENTS

The authors wish to thank PISCES technical staff for their professional skill and dedicated support. This work was supported by the US DOE under the contract DE-FG02-07ER54912, and the EURATOM mobility funds.

- <sup>1</sup>S. Takamura, N. Ohno, D. Nishijima, *et al.*, Plasma and Fusion Research **1**, 051 (2006).
- <sup>2</sup>R. Doerner, M. Baldwin, and P. Stangeby, Nuclear Fusion **51**, 043001 (2011).
- <sup>3</sup>G. Wright, D. Brunner, M. Baldwin, *et al.*, Journal of Nuclear Fusion **52**, 042003 (2012).
- <sup>4</sup>S. Kajita, S. Takamura, and N. Ohno, Nuclear Fusion **49**, 032002 (2009).
- <sup>5</sup>S. Kajita, M. Fukumoto, M. Tokitani, *et al.*, Nuclear fusion **53**, 053013 (2013).
- <sup>6</sup>D. Rudakov, C. Chrobak, R. Doerner, *et al.*, Journal of Nuclear Materials **438**, S805 (2013).
- <sup>7</sup>V. Rohde, N. Endstrasser, U. Toussaint, *et al.*, Journal of Nuclear Materials **415**, S46 (2011).
- <sup>8</sup>A. Herrmann, M. Balden, M. Laux, *et al.*, Journal of Nuclear Materials **390-391**, 747 (2009).
- <sup>9</sup>K. Hothker, W. Bieger, H. Hartwig, *et al.*, Journal of Nuclear Materials **93-94**, 785 (1980).
- <sup>10</sup>A. Stampa and H. Kruger, Journal of Physics D: Applied Physics **16**, 2135 (1983).
- <sup>11</sup>S. Wang and I. G. Browne, Review of Scientific Instruments **70**, 3583 (1999).
- <sup>12</sup>D. Nishijima, Y. Kikuchi, M. Nakatsuka, *et al.*, Fusion Science and Technology **60**, 1447 (2011).
- <sup>13</sup>F. Schwirzke, Journal of Nuclear Materials **93-94**, 780 (1980).
- <sup>14</sup>D. Aussems, D. Nishijima, C. Brandt, *et al.*, Journal of Nuclear Materials (in press).
- <sup>15</sup>J. Cowpe, R. Pilkington, J. Astin, *et al.*, J. Phys. D **42**, 165202 (2009).
- <sup>16</sup>E. Skladnik-Sadowska, K. Malinowski, M. Sadowski, *et al.*, Journal of Nuclear Materials **390-391**, 847 (2009).
- <sup>17</sup>It might be thought that the electron density can also be measured by using Stark broadening. This was proposed by Refs.<sup>29</sup>, but since other Stark constants than the ones for tungsten - which are unknown - were used, we do not think this is possible.
- <sup>18</sup>H. Griem, *Principles of plasma spectroscopy* (Cambridge University Press, 1997).
- <sup>19</sup>“Nist atomic database,” <http://www.physics.nist.gov/PhysRefdata/>, accessed: 2013-05-17.
- <sup>20</sup>R. H. Huddleston and S. L. Leonard, *Plasma Diagnostic Techniques* (New York Press, 1965).

- <sup>21</sup>J. Singh and S. Thakur, *Laser-Induced Breakdown Spectroscopy* (Elsevier, 2007).
- <sup>22</sup>S. Harilal, C. Bindhu, M. Tillack, *et al.*, *Journal of Applied Physics* **93**, 2380 (2002).
- <sup>23</sup>S. Harilal, C. V. Bindhu, V. P. N. Nampoori, *et al.*, *Applied Physics Letters* **72** (1998).
- <sup>24</sup>V. Y. Baranov, O. N. Derkach, V. G. Grishina, *et al.*, *Physics Review E* **48**, 1324 (1993).
- <sup>25</sup>C. A. J.A. Aguilera, *Appl. Phys.* **69**, S475 (1999).
- <sup>26</sup>A. Anders, *Cathodic Arcs: from Fractal Spots to Energetic Condensation* (2008).
- <sup>27</sup>D. Goebel, G. Campbell, and R. Conn, *Journal of Nuclear Materials* **121**, 277 (1984).
- <sup>28</sup>D. Nishijima and E. M. Hollmann, *Plasma Phys. Control. Fusion* **49**, 791 (2007).
- <sup>29</sup>N. Farid, C. Li, H. Wang, *et al.*, *Journal of Nuclear Materials* **433**, 80 (2013).